

Pauli-paramagnetic effects on mixed state properties in a strongly anisotropic superconductor —Application to Sr₂RuO₄—

Yuujiro Amano, Masahiro Ishihara, Masanori Ichioka,* Noriyuki Nakai, and Kazushige Machida†
Department of Physics, Okayama University, Okayama 700-8530, JAPAN

(Dated: April 9, 2022)

We study theoretically the mixed state properties of a strong uniaxially-anisotropic type II superconductor with the Pauli paramagnetic effect, focusing on their behaviors when the magnetic field orientation is tilted from the conduction layer ab plane. On the basis of Eilenberger theory, we quantitatively estimate significant contributions of the Pauli paramagnetic effects on a variety of physical observables, including transverse and longitudinal components of the flux line lattice form factors, magnetization curves, Sommerfeld coefficient, field distributions and magnetic torques. We apply these studies to Sr₂RuO₄ and quantitatively explain several seemingly curious behaviors, including the H_{c2} suppression for the ab plane direction, the larger anisotropy ratio and intensity found by the spin-flip small angle neutron scattering, and the first order transition observed recently in magnetocaloric, specific heat and magnetization measurements in a coherent and consistent manner. Those lead us to conclude that Sr₂RuO₄ is either a spin-singlet or a spin-triplet pairing with the d -vector components in the ab plane.

PACS numbers: 74.25.Uv, 74.70.Pq, 74.25.Ha, 61.05.fg

I. INTRODUCTION

Sr₂RuO₄ is well known to be a prime candidate of a chiral p -wave superconductor [1–3]. The crystal structure is same as in La₂CuO₄: a mother compound of high T_c superconductors. The normal state properties of Sr₂RuO₄ are characterized by quite a standard Landau Fermi liquid picture with a moderate mass renormalization [1] in stark contrast with the high T_c cuprates which are strange metals in every respect. Yet both have a strong two dimensional metallic conduction associated with anisotropic layered structure. In this sense Sr₂RuO₄ has a firm foundation, out of which the superconducting state develops at $T_c=1.5$ K. Thus we can safely employ a reliable theoretical framework such as Eilenberger theory that assumes a normal Fermi liquid for describing the superconducting properties under an applied field.

Recently, the research front of Sr₂RuO₄ has been greatly advanced: (1) The small angle neutron scattering (SANS) experiment [4] shows that the anisotropy ratio of the vortex lattice amounts to $\Gamma_{VL} \sim 60$ for the field orientation \mathbf{B} parallel to the ab plane. This is at odds with the H_{c2} anisotropy ratio $\Gamma_{H_{c2}} \equiv H_{c2,ab}/H_{c2,c} = 20$, where $H_{c2,ab}$ ($H_{c2,c}$) is the upper critical field H_{c2} for $\mathbf{B} \parallel ab$ ($\mathbf{B} \parallel c$), because in usual single-band superconductors $\Gamma_{VL} \sim \Gamma_{H_{c2}}$ is expected [5].

(2) The magneto-caloric effect [6], the specific heat [7] and magnetization experiments [8] detect the first order transition at $H_{c2,ab}$ in low temperatures, which is similar to superconductors with strong Pauli paramagnetic effect (PPE), such as in CeCoIn₅ [9–12].

We note that the three experiments[6–8] mentioned

above are mutually quite consistent with each others, since a certain amount of quasi-particles in the superconducting state are responsible for exhibiting the first order transition's jumps at $H_{c2,ab}$ in those thermodynamic quantities. There the same quasi-particles manifest themselves in each observable. This means that viewing from the normal side above $H_{c2,ab}$ the spin susceptibility χ_{spin} must decrease in the superconducting state. However, this expectation is in conflict with the existing Knight shift experiments by NMR [13–15] and polarized neutron scattering measurements [16]. There are no triplet pairing theories proposed so far which are able to predict the first order $H_{c2,ab}$ transition, including works by one of the present authors [17–38].

There are some other experimental reports suggesting the spin-triplet chiral p -wave superconductivity in Sr₂RuO₄. For example, the observation of half-quantized fluxoids [39], which requires multiple order parameter for the pairing function with both spin and orbital degrees of freedom active, implying the possibility of the spin-triplet pairing. The chiral domain formations and the time reversal symmetry breaking are suggested by various experimental methods [40–42]. However, a scanning Hall probe experiment [43] fails to detect the edge current expected for the chiral superconductors. In the experiments, the estimated domain sizes for each sample used in those experiments are strangely widely different from $1\mu\text{m}$ to 1mm (see Ref. 44 for detailed critical examinations on this point). Therefore, in the present status of understanding the mechanism of superconductivity in Sr₂RuO₄, the above-mentioned experimental results are mutually contradicted.

The purpose of this paper is to find a clue to resolve the contradictions, by describing the mixed state properties for a uniaxial strong anisotropic type II superconductor with PPE in the clean limit and a single band on the basis of quasi-classical Eilenberger theory. Then we

*ichioka@cc.okayama-u.ac.jp

†machida@mp.okayama-u.ac.jp

critically examine several experiments done recently on Sr_2RuO_4 and interpret the implications of those experiments in the viewpoint of the PPE. It is shown that the results are maximally consistent with the experimental data, and stimulate future theoretical and experimental studies to further understand the mechanism of the exotic superconductivity.

The Eilenberger theory is applicable for superconductors with $k_F\xi \gg 1$. For Sr_2RuO_4 this condition is well satisfied because the coherence length $\xi \sim 30\text{nm}$ and the inverse of the Fermi wave number $k_F^{-1} \sim \text{a few nm}$. In this paper we employ spin-singlet isotropic s -wave pairing for simplicity to grasp the essential features of the PPE. Among the orbital and spin parts of the pairing symmetry, essential assumption in the present theory is that the PPE works in the spin part of the pairing. In addition to the case of the spin-singlet pairing, we can expect similar behavior of PPE also in the spin-triplet pairing case if the d -vector has components in the ab plane. The assumption for the orbital part as isotropic s -wave is not intrinsic condition. Both the s -wave and the d -wave pairing show similar high field behaviors of PPE [45]. Also in the chiral p -wave pairing, we see the similar transverse components of the internal fields [46]. Thus, the replacement of the orbital part from the s -wave pairing to the chiral p -wave pairing is possible, and we expect similar behaviors there, if the PPE is active in the spin-part of the pairing.

The arrangement of this paper is as follows. In Sec. II we give the formulation based on Eilenberger theory with PPE. The spatial structures of vortices, including internal magnetic field $\mathbf{B}(\mathbf{r})$ and the paramagnetic moment $M_{\text{para}}(\mathbf{r})$, are described in Sec. III. The form factors responsible for SANS experiments are evaluated both for the longitudinal and transverse components relative to the applied field orientation in Sec. IV. In the next section V we calculate the magnetization curves and Sommerfeld coefficient $\gamma(\bar{B})$ as a function of magnetic fields to examine the first order transition's jumps of these quantities at H_{c2} . The distributions of $P(B)$ of $B(\mathbf{r})$ and $P(M)$ of $M_{\text{para}}(\mathbf{r})$ of the vortex lattice state, that are responsible for the resonance line shape of the NMR spectra, are calculated in Sec. VI. The magnetic torque curves are also evaluated in Sec. VII. We discuss intrinsic anisotropy of Γ_{VL} and $\Gamma_{H_{c2}}$ in Sec. VIII. The final section IX is devoted to conclusion and future problems. The present paper belongs to our series of papers on the magnetic field orientation dependence of uniaxial superconductors: chiral p -wave case [46] and s -wave and d -wave cases without PPE [47].

II. QUASICLASSICAL THEORY INCLUDING PAULI PARAMAGNETIC EFFECT

First, we explain the coordinate and the Fermi surface used in our calculations. We consider the case when the magnetic field orientation is tilted by θ from the c

axis towards the ab plane. We write the crystal coordinate as (a, b, c) . To describe the vortex structure, we use the coordinate $\mathbf{r} = (x, y, z)$ where z axis is set to the vortex line direction. Thus, the relation to the vortex coordinate and the crystal coordinate is given by $(x, y, z) = (a, b \cos \theta + c \sin \theta, c \cos \theta - b \sin \theta)$.

As a model of the Fermi surface, we use quasi-two dimensional Fermi surface with rippled cylinder shape. In the crystal coordinate, the Fermi velocity is assumed to be $\mathbf{v} = (v_a, v_b, v_c) \propto (\cos \phi, \sin \phi, \tilde{v}_z \sin p_c)$ at $\mathbf{p} = (p_a, p_b, p_c) \propto (p_F \cos \phi, p_F \sin \phi, p_c)$ on the Fermi surface [48]. From the Fermi surface, anisotropy ratio of the coherence lengths is estimated as

$$\Gamma \equiv \xi_c/\xi_b \sim \langle v_c^2 \rangle_{\mathbf{p}}^{1/2} / \langle v_b^2 \rangle_{\mathbf{p}}^{1/2} \sim 1/\tilde{v}_z, \quad (1)$$

where $\langle \dots \rangle_{\mathbf{p}}$ indicates an average over the Fermi surface.

The spatial structure of quasiparticles in the superconducting state is studied by the Eilenberger theory. Quasiclassical Green's functions $f(\omega_n, \mathbf{p}, \mathbf{r})$, $f^\dagger(\omega_n, \mathbf{p}, \mathbf{r})$, and $g(\omega_n, \mathbf{p}, \mathbf{r})$ are calculated in the vortex lattice states by solving Riccati equation, which is derived from the Eilenberger equation

$$\begin{aligned} \{\omega_n + i\mu B(\mathbf{r}) + \hat{\mathbf{v}} \cdot (\nabla + i\mathbf{A}(\mathbf{r}))\} f &= \Delta(\mathbf{r})g, \\ \{\omega_n + i\mu B(\mathbf{r}) - \hat{\mathbf{v}} \cdot (\nabla - i\mathbf{A}(\mathbf{r}))\} f^\dagger &= \Delta^*(\mathbf{r})g, \end{aligned} \quad (2)$$

in the clean limit with

$$\hat{\mathbf{v}} \cdot \nabla g = \Delta^*(\mathbf{r})f - \Delta(\mathbf{r})f^\dagger, \quad (3)$$

$g = (1 - ff^\dagger)^{1/2}$, $\text{Reg} > 0$, and Matsubara frequency ω_n [45, 48–50]. The paramagnetic parameter $\mu = \mu_B B_0 / \pi k_B T_c$ is proportional to the Maki parameter. We calculate the spatial structure of g in a fully self-consistent way without using Pesch's approximation [51]. We consider the case of isotropic s -wave pairing, because the paramagnetic effect does not seriously depend on the pairing function of the orbital part [45]. Normalized Fermi velocity is $\hat{\mathbf{v}} = \mathbf{v}/v_F$ with $v_F = \langle v^2 \rangle_{\mathbf{p}}^{1/2}$. We have scaled length, temperature, magnetic field, and energies in units of ξ_0 , T_c , B_0 , and $\pi k_B T_c$, respectively, where $\xi_0 = \hbar v_F / 2\pi k_B T_c$ and $B_0 = \phi_0 / 2\pi \xi_0^2$. ϕ_0 is the flux quantum. The vector potential $\mathbf{A} = \frac{1}{2} \bar{\mathbf{B}} \times \mathbf{r} + \mathbf{a}(\mathbf{r})$ is related to the internal field as $\mathbf{B}(\mathbf{r}) = \nabla \times \mathbf{A} = (B_x(\mathbf{r}), B_y(\mathbf{r}), B_z(\mathbf{r}))$ with $\bar{\mathbf{B}} = (0, 0, \bar{B})$, $B_z(\mathbf{r}) = \bar{B} + b_z(\mathbf{r})$ and $(B_x, B_y, b_z) = \nabla \times \mathbf{a}$. The spatial averages of B_x , B_y , and b_z are zero. \bar{B} is the averaged flux density of the internal field.

The pairing potential $\Delta(\mathbf{r})$ in the isotropic s -wave pairing is calculated by the gap equation

$$\Delta(\mathbf{r}) = g_0 N_0 T \sum_{0 \leq \omega_n \leq \omega_{\text{cut}}} \langle f + f^\dagger \rangle_{\mathbf{p}} \quad (4)$$

where g_0 is the pairing interaction in the low-energy band $|\omega_n| \leq \omega_c$, and N_0 is the density of states (DOS) at the Fermi energy in the normal state. g_0 is defined by the cutoff energy ω_c as $(g_0 N_0)^{-1} = \ln T + 2T \sum_{\omega_n > 0}^{\omega_c} \omega_n^{-1}$.

We carry out calculations using the cutoff $\omega_c = 20k_B T_c$. Current equation to obtain \mathbf{a} is given by

$$\nabla \times \nabla \times \mathbf{a}(\mathbf{r}) = \mathbf{j}_s(\mathbf{r}) + \nabla \times \mathbf{M}_{\text{para}}(\mathbf{r}) \quad (5)$$

with the screening current

$$\mathbf{j}_s(\mathbf{r}) = -\frac{2T}{\kappa^2} \sum_{0 \leq \omega_n} \langle \hat{\mathbf{v}} \text{Im}\{g\} \rangle_{\mathbf{p}}, \quad (6)$$

and the paramagnetic moment

$$M_{\text{para}}(\mathbf{r}) = M_0 \left(\frac{B(\mathbf{r})}{\bar{B}} - \frac{2T}{\mu \bar{B}} \sum_{0 \leq \omega_n} \langle \text{Im}\{g\} \rangle_{\mathbf{p}} \right). \quad (7)$$

Here, the normal state paramagnetic moment $M_0 = (\mu/\kappa)^2 \bar{B}$, and $\kappa = B_0/\pi k_B T_c \sqrt{8\pi N_0}$. The Ginzburg-Landau (GL) parameter κ is the ratio of the penetration depth to coherence length for $\mathbf{B} \parallel c$.

We set unit vectors of the vortex lattice as

$$\mathbf{u}_1 = c(\alpha/2, -\sqrt{3}/2), \quad \mathbf{u}_2 = c(\alpha/2, \sqrt{3}/2) \quad (8)$$

with $c^2 = 2\phi_0/(\sqrt{3}\alpha\bar{B})$ and $\alpha = 3\Gamma(\theta)$ [48], as shown in Fig. 1(a). We use the anisotropy ratio $\Gamma(\theta) \equiv \xi_y/\xi_x \sim \langle v_y^2 \rangle_{\mathbf{p}}^{1/2}/\langle v_x^2 \rangle_{\mathbf{p}}^{1/2}$, that is,

$$\Gamma(\theta) = \frac{1}{\sqrt{\cos^2 \theta + \Gamma^{-2} \sin^2 \theta}} \quad (9)$$

of the effective mass model. Supposing the case of Sr_2RuO_4 [1], we set to be $\kappa = 2.7$ and the anisotropy ratio $\Gamma(\theta = 90^\circ) = \Gamma = 60$, which is suggested by the SANS experiment [4]. By the iteration of calculations by Eqs. (2)-(7) at $T = 0.1T_c$, we obtain self-consistent solutions of $\Delta(\mathbf{r})$, $\mathbf{A}(\mathbf{r})$, and quasiclassical Green's functions.

From the selfconsistent solutions, we calculate the following physical quantities. In Eilenberger theory, free energy is given by

$$F = \kappa^2 \langle |\mathbf{B}(\mathbf{r}) - \bar{\mathbf{B}}|^2 \rangle_{\mathbf{r}} - \mu^2 \langle |\mathbf{B}(\mathbf{r})|^2 \rangle_{\mathbf{r}} + T \sum_{|\omega_n| < \omega_{\text{cut}}} \left\langle \text{Re} \left\langle \frac{g-1}{g+1} (\Delta f^\dagger + \Delta^* f) \right\rangle_{\mathbf{k}} \right\rangle_{\mathbf{r}} \quad (10)$$

when Eqs. (2) and (4) are satisfied [48]. $\langle \dots \rangle_{\mathbf{r}}$ indicates the spatial average. The magnetization is calculated as $M_{\text{total}} = \bar{B} - H$, where the external field H is given by

$$H = \left(1 - \frac{\mu^2}{\kappa^2} \right) \left(\bar{B} + \left\langle (B(\mathbf{r}) - \bar{B})^2 \right\rangle_{\mathbf{r}} / \bar{B} \right) + \frac{T}{\kappa^2 \bar{B}} \left\langle \sum_{0 \leq \omega_n} \langle \mu B_z(\mathbf{r}) \text{Im}\{g\} + \frac{1}{2} \text{Re} \left\{ \frac{(f^\dagger \Delta + f \Delta^*) g}{g+1} \right\} + \omega_n \text{Re}\{g-1\} \right\rangle_{\mathbf{k}} \right)_{\mathbf{r}}, \quad (11)$$

from Doria-Gubernatis-Rainer scaling [52, 53]. The paramagnetic and diamagnetic components of the magnetization are, respectively, $M_{\text{para}} = \langle M_{\text{para}}(\mathbf{r}) \rangle_{\mathbf{r}}$ and $M_{\text{dia}} =$

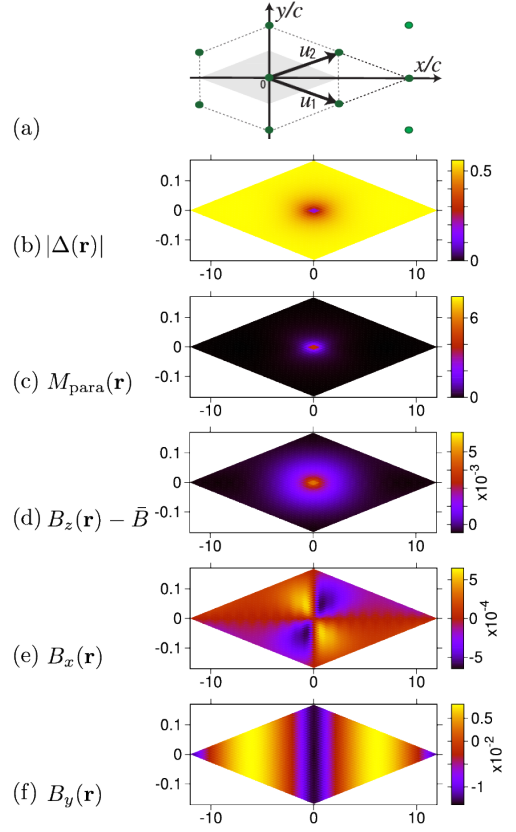


FIG. 1: (Color online) (a) Unit vectors \mathbf{u}_1 and \mathbf{u}_2 of the vortex lattice. Circles indicate vortex centers. Gray region is a unit cell of our calculations. (b) $|\Delta(\mathbf{r})|$. (c) $M_{\text{para}}(\mathbf{r})$. (d) $B_z(\mathbf{r}) - \bar{B}$. (e) $B_x(\mathbf{r})$. (f) $B_y(\mathbf{r})$. In (b)-(f), we show density plot within a unit cell, when $\theta = 89^\circ$ at $\bar{B} = 1.5$ and $\mu = 0.04$.

$M_{\text{total}} - M_{\text{para}}$. As the resonance line shape of the NMR spectrum for the Knight shift, we calculate the distribution function $P(M) = \langle \delta(M - M_{\text{para}}(\mathbf{r})) \rangle_{\mathbf{r}}$ from the spatial structure of $M_{\text{para}}(\mathbf{r})$. On the other hand, in the case of negligible hyperfine coupling, the NMR signal shows ‘‘Redfield pattern’’ given by the distribution function $P(B) = \langle \delta(B - B(\mathbf{r})) \rangle_{\mathbf{r}}$ calculated from the internal field $B(\mathbf{r})$.

When we calculate the electronic states, we solve Eq. (2) with $i\omega_n \rightarrow E + i\eta$. The local density of states (LDOS) is given by $N(\mathbf{r}, E) = N_\uparrow(\mathbf{r}, E) + N_\downarrow(\mathbf{r}, E)$, where

$$N_\sigma(\mathbf{r}, E) = N_0 \langle \text{Re}\{g(\omega_n + i\sigma\mu B, \mathbf{k}, \mathbf{r})|_{i\omega_n \rightarrow E + i\eta}\} \rangle_{\mathbf{k}} \quad (12)$$

with $\sigma = 1$ (-1) for up (down) spin component. We typically use $\eta = 0.01$. The DOS is obtained by the spatial average of the LDOS as $N(E) = N_\uparrow(E) + N_\downarrow(E) = \langle N(\mathbf{r}, E) \rangle_{\mathbf{r}}$. We consider the \bar{B} -dependence of the Sommerfeld coefficient of the specific heat given by the zero-energy DOS $\gamma(\bar{B}) = N(E=0)/N_0$, and the paramagnetic susceptibility $\chi_{\text{spin}}(\bar{B}) = \langle M_{\text{para}}(\mathbf{r}) \rangle_{\mathbf{r}}/M_0$. These are normalized by the normal state values.

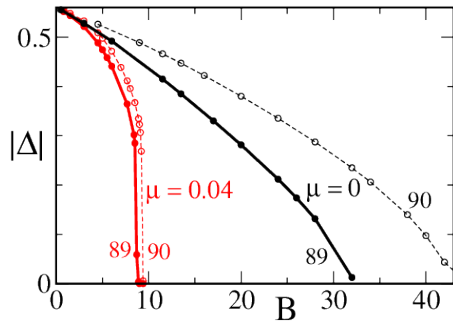


FIG. 2: (Color online) (a) \bar{B} -dependence of the pair potential when $\theta = 89^\circ$ (solid lines) and $\theta = 90^\circ$ (dashed lines). Spatial averaged values of $|\Delta(\mathbf{r})|$ are presented for $\mu = 0$ and $\mu = 0.04$. The latter ($\mu = 0.04$) exhibits first order transitions for both 89° and 90° .

III. SPATIAL STRUCTURES OF VORTICES

To discuss \bar{B} -dependence of the internal field distribution $\mathbf{B}(\mathbf{r}) = \nabla \times \mathbf{A}$, we consider flux line lattice (FLL) form factors $\mathbf{F}(\mathbf{q}_{h,k}) = (F_x(h,k), F_y(h,k), F_z(h,k))$, which is obtained by Fourier transformation of the internal field distribution as $\mathbf{B}(\mathbf{r}) = \sum_{h,k} \mathbf{F}(\mathbf{q}_{h,k}) \exp(i\mathbf{q}_{h,k} \cdot \mathbf{r})$ with wave vector $\mathbf{q}_{h,k} = h\mathbf{q}_1 + k\mathbf{q}_2$. h and k are integers. Unit vectors in reciprocal space are given by $\mathbf{q}_1 = (2\pi/c)(1/\alpha, -1/\sqrt{3})$ and $\mathbf{q}_2 = (2\pi/c)(1/\alpha, 1/\sqrt{3})$. The z -component $|F_z(h,k)|^2$ from $B_z(\mathbf{r})$ gives the intensity of conventional non-spin flip SANS. The transverse component, $|F_{\text{tr}(h,k)}|^2 = |F_x(h,k)|^2 + |F_y(h,k)|^2$, is accessible by spin-flip SANS experiments [4, 54].

First, we study the vortex states when the magnetic field orientation is tilted by 1° from the ab plane ($\theta = 89^\circ$). In Fig. 1, we show the calculated spatial structures within a unit cell of vortex lattice at $\bar{B} = 1.5$ and $\mu = 0.04$. The pair potential $\Delta(\mathbf{r})$ has phase winding 2π at the vortex center, and the amplitude $|\Delta(\mathbf{r})|$ in Fig. 1(b) is suppressed at the vortex core. The paramagnetic moment $M_{\text{para}}(\mathbf{r})$ in Fig. 1(c) is suppressed outside of the vortex core. $M_{\text{para}}(\mathbf{r})$ appears within the narrow region around the vortex core and has a large peak at the vortex center. As shown in Fig. 1(d), the z -component of internal field, $B_z(\mathbf{r})$, has a peak at the vortex center, and decreases as a function of the distance from the center. The peak height of $B_z(\mathbf{r})$ is enhanced by the contribution of $M_{\text{para}}(\mathbf{r})$ at the vortex core [45]. The vortex state has a conventional spatial structure in the vortex lattice also when $\bar{\mathbf{B}}$ is tilted from the ab plane, if length is scaled by the effective coherence length in each direction. When $\bar{\mathbf{B}}$ is tilted from the ab plane, the transverse components $B_x(\mathbf{r})$ and $B_y(\mathbf{r})$ appear in the internal field distribution, as shown in Figs. 1(e) and 1(f). The magnitude of $B_y(\mathbf{r})$ is larger than that of $B_x(\mathbf{r})$. The stream lines of $B_y(\mathbf{r})$ in Fig. 1(f) flow towards $-y$ direction along vertical stripe region connecting vortex cores. Between the neighbor stripe regions, the stream

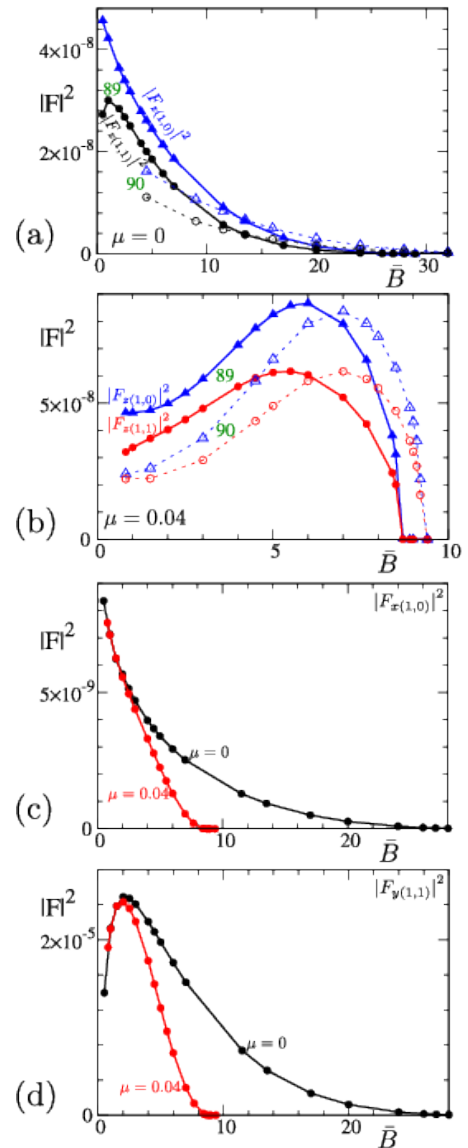


FIG. 3: (Color online) \bar{B} -dependence of the FLL form factors. (a) $|F_{z(1,0)}|^2$ and $|F_{z(1,1)}|^2$ for $\mu = 0$, when $\theta = 89^\circ$ (solid lines) and 90° (dashed lines). (b) The same as (a), but for $\mu = 0.04$. (c) $|F_{x(1,0)}|^2$ for $\mu = 0$ and 0.04 when $\theta = 89^\circ$. (d) $|F_{y(1,1)}|^2$ for $\mu = 0$ and 0.04 when $\theta = 89^\circ$.

line flows towards $+y$ -direction. The weak contribution of $B_x(\mathbf{r})$ in Fig. 1(e) indicates that the stream lines have weak counter-clock-wise (clock-wise) winding at positive- x (negative- x) region near vortex core. These stream line structures of the transverse field is qualitatively the same as those obtained by London theory [55], and as those in a chiral p -wave pairing [46].

When the paramagnetic effect is not considered ($\mu = 0$), the upper-critical field is $H_{c2,c} = 0.56$ for $\bar{\mathbf{B}} \parallel c$ and $H_{c2,ab} = 43$ for $\bar{\mathbf{B}} \parallel ab$, reflecting large anisotropy Γ . Figure 2 presents the amplitude of the pair potential as a function of \bar{B} . In the case $\mu = 0.04$, the paramagnetic

pair-breaking is negligible for $\bar{\mathbf{B}} \parallel c$ so that $H_{c2,c}$ is unchanged. However, for $\bar{\mathbf{B}} \parallel ab$, the paramagnetic pair breaking becomes eminent at high fields and limits the upper critical field to $H_{c2,ab} = 9.1$. The phase transition at $H_{c2,ab}$ becomes first order as coinciding with the observation in Sr_2RuO_4 at low temperatures [6–8].

For the field orientation tilted by 1° away from the ab plane, namely $\theta = 89^\circ$, H_{c2} is suppressed from $H_{c2,ab}$ at $\theta = 90^\circ$ as seen from Fig. 2. It is noted that those H_{c2} suppressions are quite different: While in the $\mu = 0$ case $H_{c2}(\theta = 89^\circ)/H_{c2}(\theta = 90^\circ) = 32/43 \sim 0.74$, approximately satisfying the expectation based on our effective mass model; $\Gamma(\theta = 89^\circ)/\Gamma(\theta = 90^\circ) \sim 0.69$, the H_{c2} suppression in the $\mu = 0.04$ case is very small and remains first order. This is because H_{c2} is determined by the PPE and controlled by the Pauli paramagnetic critical field $H_p(\theta)$ which has a weak θ dependence [45]. This point will be discussed later in connection with the nature of the phase transitions.

IV. FLUX LINE LATTICE FORM FACTORS

A. Longitudinal component

We discuss the \bar{B} -dependence of the FLL form factor for $\theta = 90^\circ$ and 89° . Figures 3(a) and 3(b) present the \bar{B} -dependence of $|F_{z(1,1)}|^2$ and $|F_{z(1,0)}|^2$. These correspond to the intensity of the non-spin-flip SANS experiments. When $\mu = 0$ in Fig. 3(a), $|F_{z(1,1)}|^2$ and $|F_{z(1,0)}|^2$ show exponential decay as a function of \bar{B} . However, when $\mu = 0.04$ in Fig. 3(b), both $|F_{z(1,0)}|^2$ and $|F_{z(1,1)}|^2$ increase towards a maximum at $\bar{B} \sim 7$ for $\theta = 90^\circ$. This increasing behavior is due to the enhancement of the paramagnetic moment at the vortex, which enhances the peak of $B_z(\mathbf{r})$. This mechanism[45] was discussed to explain the \bar{B} -dependence of the SANS intensity in CeCoIn_5 [12, 56] and $\text{TmNi}_2\text{B}_2\text{C}$ [57]. Compared to the case of $\theta = 90^\circ$, the intensities of $|F_{z(h,k)}|^2$ are more enhanced for $\theta = 89^\circ$ at low fields. This is because the intensity $|F_{z(h,k)}|^2$ is roughly related to the effective GL parameter κ_θ as $|F_{z(h,k)}|^2 \propto \kappa_\theta^{-2}$. By the anisotropy of $\hat{\mathbf{v}}$ in Eq. (6), $\kappa_\theta \sim \kappa\Gamma(\theta)$ for the field orientation θ . Thus, $\kappa_{89^\circ} < \kappa_{90^\circ}$. At high fields, the peak position of $|F_{z(h,k)}|^2$ is shifted to $\bar{B} \sim 6$ when $\theta = 89^\circ$, reflecting the θ -dependence of anisotropic H_{c2} .

B. Transverse components

The \bar{B} -dependence of the transverse component is shown in Figs. 3(c) and 3(d). As for (1,0) spot, $|F_{\text{tr}(1,0)}|^2 \sim |F_{x(1,0)}|^2$ since $|F_{y(1,0)}|^2 < 10^{-11}$. $|F_{x(1,0)}|^2$ decreases monotonically as a function of \bar{B} . As for (1,1) spot, $|F_{\text{tr}(1,1)}|^2 \sim |F_{y(1,1)}|^2$ since $F_{x(1,1)} \sim 0$. $|F_{y(1,1)}|^2$ decreases as a function of \bar{B} , after it increases at low \bar{B} . As in the chiral p -wave pairing [46], $|F_{y(1,1)}|^2$ has large

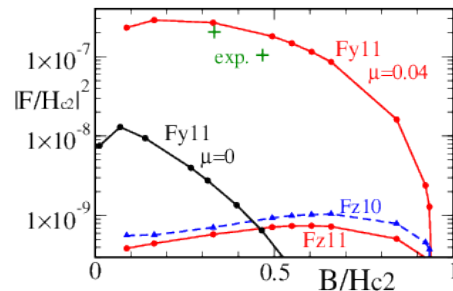


FIG. 4: (Color online) \bar{B} -dependence of the FLL form factors when $\theta = 89^\circ$. We plot renormalized values $|F_{y(1,1)}/H_{c2,ab}|^2$ as a function of $\bar{B}/H_{c2,ab}$ for $\mu = 0.04$ and 0. The points + indicate experimental values[4] on Sr_2RuO_4 . We also present $|F_{z(1,0)}/H_{c2,ab}|^2$ and $|F_{z(1,1)}/H_{c2,ab}|^2$. The vertical axis is a logarithmic scale.

intensity, compared with $|F_{x(1,0)}|^2$ and $|F_{z(h,k)}|^2$. This is consistent to the fact that only the spin-flip scattering at (1,1) is observed in the SANS experiment[4] on Sr_2RuO_4 . From Figs. 3(c) and 3(d), we see that the enhancement due to the paramagnetic effect does not appear in the transverse component $|F_{\text{tr}(h,k)}|^2$. Rather $|F_{\text{tr}(h,k)}|^2$ decreases rapidly at higher fields, reflecting the paramagnetic suppression of superconductivity.

For the quantitative comparison with the experimental data[4] in Sr_2RuO_4 , we discuss the form factors and \bar{B} in unit of $H_{c2,ab}$ as plotted in Fig. 4. In the case $\mu = 0.04$, $|F_{y(1,1)}/H_{c2,ab}|^2$ is larger because $H_{c2,ab}$ is smaller. In Fig. 4, we also show the experimental data[4] on Sr_2RuO_4 with $H_{c2,ab} = 1.5[\text{T}]$, i.e., $F_{\text{tr}(1,1)} = 0.677[\text{mT}]$ at $\bar{B} = 0.5[\text{T}]$ and $F_{\text{tr}(1,1)} = 0.485[\text{mT}]$ at $\bar{B} = 0.7[\text{T}]$. The magnitude of $|F_{y(1,1)}/H_{c2,ab}|^2$ in experimental data can be quantitatively reproduced in the case $\mu = 0.04$ including the effect of $H_{c2,ab}$ suppression. From Fig. 4, we also see that 10^{-2} -times finer resolution is necessary in the SANS experiment to observe the spot of $|F_{z(h,k)}|^2$ for the non-spin-flip scattering, which is expected to be an increasing function of \bar{B} at the middle field range.

The θ -dependence of the $|F_{y(1,1)}|^2$ is presented in Fig. 5. As a function of θ , $|F_{y(1,1)}|^2$ increases until a peak near 90° . After the peak it decreases rapidly towards zero just at 90° . At low enough field $\bar{B} = 1.5$, $|F_{y(1,1)}|^2$ shows similar behavior both for $\mu = 0$ and 0.04. With increasing \bar{B} , the peak position is shifted to higher θ , and the amplitude is decreased. At higher fields such as $\bar{B} = 13.5$, $|F_{y(1,1)}|^2$ becomes very small for $\mu = 0$. However, these high field regions vanish for $\mu = 0.04$ because of high-field suppression of superconductivity. For the quantitative comparison, Fig. 5(c) shows renormalized values $|F_{y(1,1)}/H_{c2,ab}|^2$ in a logarithmic scale with the SANS results on Sr_2RuO_4 for two cases $\bar{B}/H_{c2,ab} \sim 0.33$ ($\bar{B} = 3.0B_0$ and $0.5[\text{T}]$) and $\bar{B}/H_{c2,ab} \sim 0.5$ ($\bar{B} = 4.5B_0$ and $0.7[\text{T}]$). We see that the experimental data are well fit by the theory for $\mu = 0.04$ near $\theta = 89^\circ$. The theoretical values for $\mu = 0$ is very small compared to the SANS

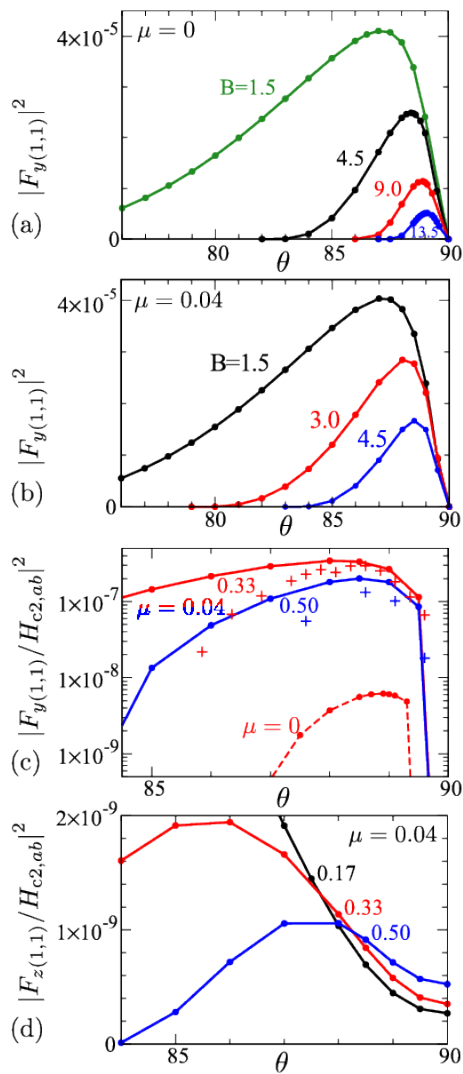


FIG. 5: (Color online) Field orientation θ -dependence of the transverse FLL form factor. (a) $|F_{y(1,1)}/H_{c2,ab}|^2$ as a function of θ for $\mu = 0$ at $\bar{B} = 1.5, 4.5, 9.0,$ and 13.5 . (b) $|F_{y(1,1)}/H_{c2,ab}|^2$ as a function of θ for $\mu = 0.04$ at $\bar{B} = 1.5, 3.0,$ and 4.5 . (c) $|F_{y(1,1)}/H_{c2,ab}|^2$ in a logarithmic scale as a function of θ for $\mu = 0.04$ at $\bar{B}/H_{c2,ab} \sim 0.33$ and 0.5 ($\bar{B} = 3.0$ and 4.5). The points $+$ indicate experimental values[4] on Sr_2RuO_4 at $0.5[\text{T}]$ and $0.7[\text{T}]$. We also plot $|F_{y(1,1)}/H_{c2,ab}|^2$ for $\mu = 0$ at $\bar{B} = 9.0$ ($\bar{B}/H_{c2,ab} = 0.21$). (d) θ dependence of the longitudinal FLL form factor $|F_{z(1,1)}/H_{c2,ab}|^2$ for $\mu = 0.04$ at $\bar{B}/H_{c2,ab} = 0.17, 0.33,$ and 0.50 .

results.

We also plot the longitudinal component $|F_{z(1,1)}/H_{c2,ab}|^2$ for $\mu = 0.04$ in Fig. 5(d) that is not yet observed in Sr_2RuO_4 . It is seen that $|F_{z(1,1)}/H_{c2,ab}|^2$ grows as \bar{B} increases at $\theta = 90^\circ$ because of PPE, as seen in Fig. 3(b). At a low field $\bar{B}/H_{c2,ab} = 0.17$, $|F_{z(1,1)}|^2$ monotonically increases when θ decreases, since $|F_{z(1,1)}|^2 \propto \kappa_\theta^{-2}$. We notice that the longitudinal components of the form factor are already observed

for $\theta = 0$, i.e., $H \parallel c$ [58]. The detailed analysis of those form factors has not done yet, but it seems to be similar to the results for the square lattice for the d -wave case [59]. For larger fields $\bar{B}/H_{c2,ab} = 0.33$ and 0.50 , it takes a peak at finite θ because the effective magnetic field \bar{B}/H_{c2} becomes large as θ decreases from 90° . Then $F_{z(1,1)}$ vanishes ultimately towards H_{c2} where the order parameter is zero. This peak behavior in $F_{z(1,1)}$ is similar to those shown in Fig. 3(b) where the longitudinal components as a function of \bar{B} exhibit peaks just below H_{c2} .

V. JUMPS AT FIRST ORDER H_{c2} TRANSITION

A. Magnetization curves

We calculate the magnetization curves for $\theta = 89^\circ$ and 90° both in the cases of $\mu = 0$ and $\mu = 0.04$ at $T = 0.1T_c$ as shown in Figs. 6(a) and 6(b). In the $\mu = 0$ case, $M_{\text{total}}(\bar{B})$ corresponds to that of an ordinary type II superconductor, because $M_{\text{total}}(\bar{B})$ comes exclusively from the orbital diamagnetism due to the orbital current. Since the second order transition occurs at H_{c2} in this case, $M_{\text{total}}(\bar{B})$ smoothly becomes zero.

As seen from Fig. 6(b) in $\mu = 0.04$, $M_{\text{total}}(\bar{B})$ exhibits the jumps ΔM_{total} at H_{c2} both for $\theta = 89^\circ$ and 90° , corresponding to the first order transition. The magnetization jump ΔM_{total} consists of the two components; the orbital diamagnetism ΔM_{dia} and the spin paramagnetism ΔM_{para} . For $\theta = 90^\circ$ $M_{\text{para}} = 1.3 \times 10^{-3}$ and $M_{\text{dia}} = -0.7 \times 10^{-4}$ at $\bar{B} = H_{c2} = 9.1$. Thus ΔM_{total} is dominated by the spin paramagnetic component. Since at $\bar{B} = H_{c2}$, $M_{\text{normal}} = 2.0 \times 10^{-3}$, the relative jump $\Delta M_{\text{total}}/M_{\text{normal}} = 38.5\%$. As seen from Fig. 6(b), the $\theta = 89^\circ$ case also gives rise to a similar ΔM_{total} value.

This number is favorably compared with the experimental value $\Delta M_{\text{total}}/M_{\text{normal}} = 15\%$ in Sr_2RuO_4 at low temperatures [8]. A slightly larger value of $\Delta M_{\text{total}}/M_{\text{normal}}$ in our calculation can be remedied by considering the multiband effect because near H_{c2} the minor band may be almost in the normal state where the minor gap is already vanishing. The minor band contribution can be estimated as $\Delta M_{\text{total}}/(M_{\text{normal}} + M_{\text{minor}}) \sim 19\%$ because the DOS of the minor band is a half of the total DOS.

As seen from Fig. 6(c), the contribution of the orbital diamagnetism M_{dia} to the first order jump amounts to $\Delta M_{\text{dia}} = -0.7 \times 10^{-4}$. The weight of the jump, $\Delta M_{\text{dia}}/M_{\text{normal}} = 3.5\%$, is an order too smaller than the observed value. Thus without PPE it is impossible to understand the large magnetization jump. We also point out that the magnetization curve for the chiral p -wave case (see Fig. 6(a) in Ref. 46) is almost same as in usual type II superconductor without PPE shown in Fig. 6(a). Thus, if we assume a hypothetical first order transition at $H_{1\text{st}}$, then $H_{1\text{st}} \sim 0.25H_{c2}$ to account for the magnetization jump $\Delta M_{\text{total}}/M_{\text{normal}} = 15\%$. So far there is no

known theory to explain the first order transition in the chiral p -wave pairing.

B. Specific heat jump at H_{c2}

We show the calculated results of the DOS at the Fermi level at low temperature $T = 0.1T_c$ in Fig. 6(d), which corresponds to the Sommerfeld coefficient $\gamma(\bar{B})$, namely C/T at low temperatures in the superconducting state. It is known by the explicit calculations [45] that $\gamma(\bar{B})$ is approximately scaled to the spin susceptibility $\chi_{\text{spin}}(\bar{B})$ as is seen from Fig. 6(d). This is because both quantities $\chi_{\text{spin}}(\bar{B})$ and $\gamma(\bar{B})$ come from the same DOS of the quasi-particles near the Fermi level [45]. In fact the experimental value[7] of the specific heat jump at H_{c2} is $\Delta\gamma/\gamma_{\text{normal}} \sim 10\%$, roughly coinciding with $\Delta M_{\text{total}}/M_{\text{normal}} = 15\%$ mentioned above. As is seen from Fig. 6(d), the jump of $\gamma(\bar{B})$ is slightly smaller than that of χ_{spin} because two quantities are not exactly identical where the former is an integration of the DOS over $\mu_B \bar{B}$ while the latter is the DOS at the Fermi level.

It should be noted that the entropy jump[6] probed by the magneto-caloric measurement is consistent with the specific heat jump as discussed in Ref. [7], meaning that three experiments, magneto-caloric, specific heat and magnetization are mutually consistent with each other. If this identification is true, the Knight shift should decrease as shown in Fig. 6(d), which is contrasted with the claim by the NMR experiments[13–15] where the Knight shift remains unchanged, irrespective to nuclear species (^{17}O , ^{87}Sr , ^{101}Ru , and ^{99}Ru), the field orientations and the field values. This is quite at odds in the present analysis.

VI. FIELD DISTRIBUTIONS

Figures 7(a) and 7(b) display the field evolutions of $P(B)$ and $P(M)$ together with the contour maps of $B_z(\mathbf{r})$ and $M_{\text{para}}(\mathbf{r})$ within a unit cell. It is seen that as increasing field towards H_{c2} the vortex core site and its surrounding sites exclusively accommodate the paramagnetic moments induced by PPE where the highest B_z and M_{para} are situated. The mean value of $P(M)$ equals χ_{spin} in Fig. 6(d). At $\bar{B}=8.5$, due to the contributions of the paramagnetic moment enhanced at the vortex core, $P(B)$ and $P(M)$ have larger weights near the small peak at highest edges, whose positions of highest edge exceed \bar{B} and M_0 , respectively. Thus the so-called Redfield pattern $P(B)$ is strongly modified from the standard asymmetric distribution in ordinary superconductors [60, 61], such as Nb [62]. This is also true for $P(M)$ where the asymmetric pattern is modified so that the higher M range of the spectrum is enhanced.

Those asymmetric spectrum patterns should be observed by NMR experiments, where neither asymmetric $P(B)$ nor $P(M)$ patterns are not observed in any nuclear

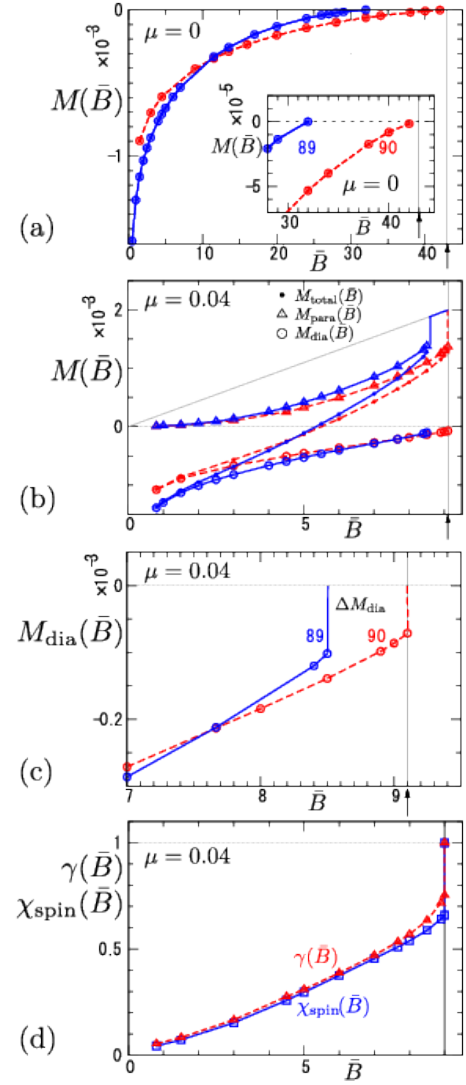


FIG. 6: (Color online) \bar{B} -dependence of the magnetization. (a) $M_{\text{total}}(\bar{B}) = M_{\text{dia}}(\bar{B})$ for $\mu = 0$, when $\theta = 89^\circ$ (solid line) and 90° (dashed line). In the inset $M_{\text{total}}(\bar{B})$ is enlarged near H_{c2} . (b) $M_{\text{total}}(\bar{B})$, $M_{\text{para}}(\bar{B})$ and $M_{\text{dia}}(\bar{B})$ for $\mu = 0.04$ when $\theta = 89^\circ$ (blue solid lines) and 90° (red dashed lines). (c) $M_{\text{dia}}(\bar{B})$ is focused near H_{c2} for $\theta = 89^\circ$ and 90° to see the jumps of ΔM_{dia} at H_{c2} . (d) The scaling behaviors of $\gamma(\bar{B})$ and $\chi_{\text{spin}}(\bar{B})$ for $\theta = 90^\circ$. The jumps of $\Delta\gamma$ and $\Delta\chi_{\text{spin}}$ relative to its normal values are seen at the first order H_{c2} transition.

species (^{17}O , ^{87}Sr , ^{101}Ru , and ^{99}Ru) for $\bar{\mathbf{B}} \parallel ab$. They remain the same patterns as in the normal state [13]. Note that the characteristics in Fig. 7 are indeed observed in CeCoIn_5 [11]. On the other hand, for $\bar{\mathbf{B}} \parallel c$, a clear Redfield pattern is observed by the muon spin resonance experiment [63]. By analyzing this pattern they correctly reduce the vortex lattice symmetry, namely a square lattice that is confirmed later by SANS experiments [58].

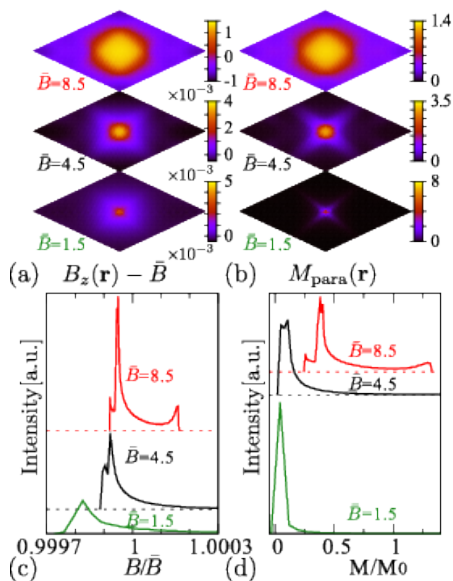


FIG. 7: (Color online) Topographic maps of (a) $B_z(\mathbf{r}) - \bar{B}$ and (b) $M_{\text{para}}(\mathbf{r})$ within one unit cell at $\bar{B} = 1.5, 4.5$ and 8.5 for $\mu = 0.04$ and $\theta = 90^\circ$. The field distribution (c) $P(B)$ and (d) $P(M)$ associated to (a) and (b), respectively.

VII. MAGNETIC TORQUE

Since we obtained the self-consistent solutions of Eilenberger equation under a given T and \bar{B} , it is not difficult to calculate the magnetic torque $\tau(\theta) = dF/d\theta$ by using the free energy F as a function of θ . The obtained free energy $F(\theta)$ is displayed in Figs. 8(a) and 8(b) for $\mu = 0$ and $\mu = 0.04$, respectively. It is seen that for both cases all the free energy curves smoothly become zero when θ decreases away from $\theta = 90^\circ$, meaning that those are all second order H_{c2} transitions in the field range $\bar{B} \leq H_{c2}(\theta = 88^\circ)$.

Figures 8(c) and 8(d) show the magnetic torque curves $\tau(\theta)$ for $\mu = 0$ and $\mu = 0.04$, respectively. It is seen from those that the sharp minima in $\tau(\theta)$ for both cases are located just near $\theta = 90^\circ$. The fact that the minimum position θ_{min} in $\tau(\theta)$ is confined near $\theta = 90^\circ$ is due to the large uniaxial anisotropy $\Gamma = 60$. This behavior is easily fit by the Kogan torque formula [64] based on the London theory:

$$\tau(\theta) \propto \frac{\sin 2\tilde{\theta}}{\sqrt{\cos^2 \tilde{\theta} + \Gamma^2 \sin^2 \tilde{\theta}}} \ln \frac{\tilde{\eta}\Gamma H_{c2,c}}{\bar{B}\sqrt{\cos^2 \tilde{\theta} + \Gamma^2 \sin^2 \tilde{\theta}}} \quad (13)$$

with $\tilde{\theta} = 90^\circ - \theta$, where $\tilde{\eta}$ is a coefficient with the order ~ 1 . The minimum θ_{min} occurs at $\theta_{\text{min}} = 88.7^\circ$ for $\Gamma = 60$ with $\eta = 1.5$, which is consistent with our Eilenberger solution. It should be noticed that at lower fields $\tau(\theta)$ is insensitive of the presence or absence of PPE according to our results in Figs. 8(c) and 8(d). Thus, both

cases are described by the Kogan formula which only depends on Γ . In fact the minima observed experimentally show $\theta_{\text{min}}^{\text{exp}} \sim 89^\circ$ at higher fields, which becomes $\theta_{\text{min}}^{\text{exp}} \sim 88^\circ$ towards lower fields (see Fig. 3(d) by Ref. 8). Also in the numerical calculation with $\Gamma = 60$, θ_{min} shows similar weak \bar{B} -dependence. Thus the torque data support the large uniaxial anisotropy with $\Gamma = 60$ for Sr_2RuO_4 . We note that if we choose $\Gamma = 20$ as indicated by $H_{c2,ab}/H_{c2,c} \sim 20$, we find $\theta_{\text{min}} \sim 87^\circ$ which is far off the experimental data[8] within the present experimental accuracy. Thus the intrinsic anisotropy of Sr_2RuO_4 should be $\Gamma = 60$ rather than $\Gamma = 20$. The latter number is now understood as arising from the suppressed H_{c2} by PPE.

Since the magnetic torque is related to the transverse components of the internal field, it is interesting to compare the $|\tau(\theta)|$ curves with the form factor $|F_{y(1,1)}|^2$ for both $\mu = 0$ and $\mu = 0.04$ as shown in Figs. 9 (a) and 9(b). An approximate scaling relationship between them is seen from both cases. In particular, the maximum position θ_{max} in both quantities yields the same value for the higher field data. This is indeed seen experimentally (see Figs. 3(c) and 3(d) in Ref. 8).

In Fig. 10(a) we compare the theoretical torque curves and corresponding experimental data [8] for selected field values. It is seen from it that they show a good agreement, in particular in the higher field data, including the maximum angles and vanishing angles of the torque curves. The highest field theoretical curve $\bar{B}=8.6$ exhibits a first order jump at $\theta = 89.1^\circ$, which nicely coincides with the data at 1.4[T]. On the other hand, the lower field data at 0.2[T] show a deviation from the theoretical curve $\bar{B}=1.5$ in their maximum angles. This may come from the multi band effect, which will be discussed in the forthcoming paper [65].

In Fig. 10(b) we summarize our maximum angle data coming from the torque curves and the transverse form factors and compare those with the experimental data [4, 8]. As already indicated in Fig.9, the discrepancies of the maximum angles between the torque and form factor occur when the field is lowered. Since the form factor data at lower fields is lacking at present, we cannot judge whether or not those discrepancies are strengthened further by future SANS experiments. Except for those lowest field data the overall agreement seems to be satisfactory. In other words, the present single band theory gives a reasonable explanation to those data.

VIII. DISCUSSIONS ON PHASE DIAGRAM AND INTRINSIC ANISOTROPY

In previous sections, the vortex lattice anisotropy $\Gamma_{\text{VL}}(\theta) \equiv \alpha/3$ in the definition of Eq. (8) is assumed to be given by the effective mass model in Eq. (9). We also perform calculations to determine $\Gamma_{\text{VL}}(\theta)$ by the minimization procedure of the free energy, which is much time consuming process compared above. The results

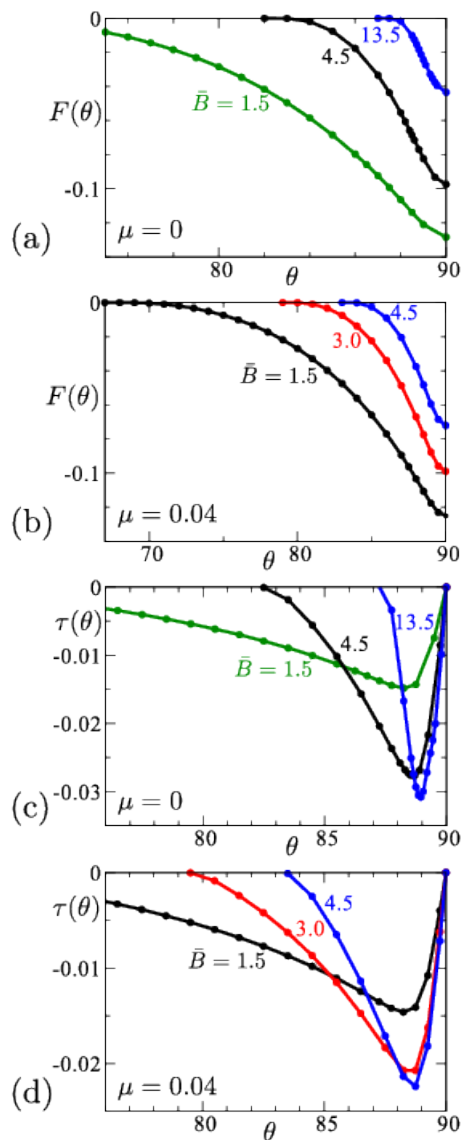


FIG. 8: (Color online) The θ -dependences of the free energies for various fields \bar{B} . (a) $\mu = 0$ and (b) $\mu = 0.04$. The corresponding torque curves $\tau(\theta) = dF/d\theta$. (c) $\mu = 0$ and (d) $\mu = 0.04$.

are shown in Fig. 11(a). It is seen that this yields a slightly larger $\Gamma_{\text{VL}}(\theta)$ compared with the effective mass model shown by a line there around $\theta = 90^\circ \pm 2^\circ$ region, beyond which all data points tend to coincide with a line of the effective mass model. We confirm that this deviation of $\Gamma_{\text{VL}}(\theta)$ does not alter our results in previous sections in a serious way.

We note that, as presented in Fig. 11(a), experimental data [4] also slightly deviate from the effective mass model for $87^\circ < \theta < 89^\circ$, which is similar to $\Gamma_{\text{VL}}(\theta)$ by the free energy minimum. This behavior will be discussed in a forth coming paper based on multiband model [65]. From the θ -dependence of $\Gamma_{\text{VL}}(\theta)$ in Fig. 11(a), the in-

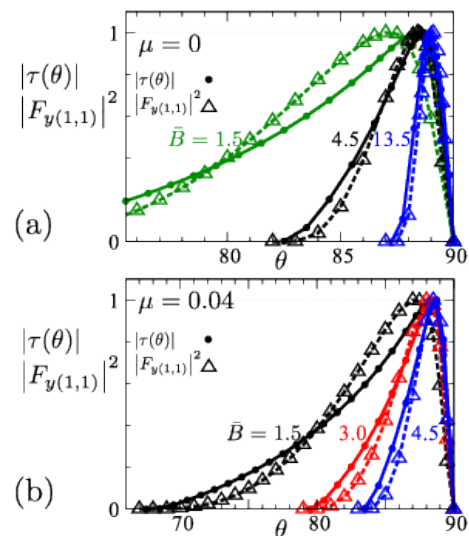


FIG. 9: (Color online) The scaling behaviors between $|F_{y(1,1)}|^2$ and $|\tau(\theta)|$ as a function of θ . (a) $\mu = 0$ and (b) $\mu = 0.04$. Magnitude of each quantity is scaled by the maximum value.

trinsic uniaxial anisotropy of the system can be identified as $\Gamma = 60$. This number just corresponds to the Fermi velocity anisotropy of the β band, since the band-dependent anisotropies are estimated as $\Gamma_\alpha = 117$, $\Gamma_\beta = 57$, and $\Gamma_\gamma = 174$ for the α , β , and γ Fermi-surface sheets, respectively, according to the dHvA experiments[1]. We emphasize that this is not accidental, if the β band plays a major role to govern the mixed state properties of the total system in high fields, further suggesting that the γ band plays a secondary role, which is contrary to what many previous works claim, such as Nomura and Yamada [20].

According to the present analysis, the $H_{c2,ab}$ suppression is explained by PPE. We evaluate $H_{c2}(\theta)$ for each θ by the estimate of the critical field where the order parameters vanish on raising \bar{B} , as done in Fig. 2. The θ -dependence of $H_{c2}(\theta)/H_{c2,c}$ is presented in Figs. 11(b) and 11(c), where the filled (empty) symbols correspond to the first (second) order transitions. Our calculation shows that the first order transitions only occur for $\theta = 89^\circ, 90^\circ, 91^\circ$, beyond which all H_{c2} transitions become second order as displayed in Figs. 11(b) and 11(c). This is consistent to experimental data [8] presented in the figures. There, in Sr_2RuO_4 the first order transitions occur within $90^\circ \pm 2^\circ$. The first order transition near the ab plane appears because the effective paramagnetic parameter $\tilde{\mu}(\theta) = \mu\Gamma(\theta)$ in Eq. (A2) exceeds the critical value $\mu_{\text{cr}} \sim 1.7$ for the first order transition only for the angles $89^\circ < \theta < 91^\circ$.

As seen from Figs. 11(b) and 11(c), $H_{c2}(\theta)/H_{c2,c}$ values by the numerical calculations are well fit by a simple function [66] in Eq. (A3) with $\mu = 0.04$, explained in Appendix. The values of $H_{c2}(\theta)/H_{c2,c}$ are slightly un-

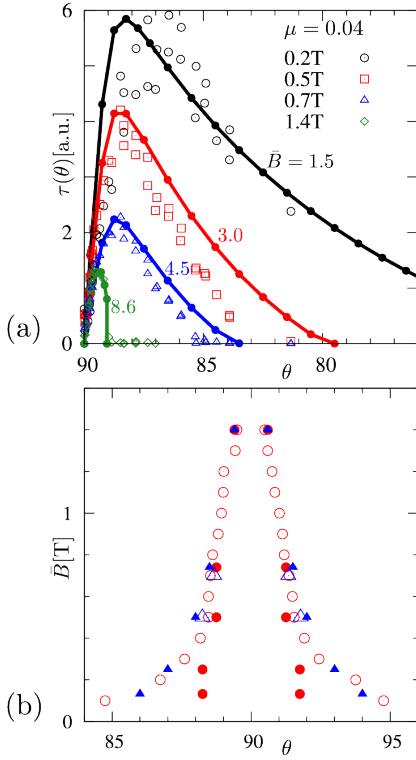


FIG. 10: (Color online) (a) Comparison with the theoretical torque curves $|\tau(\theta)|$ for $\bar{B} = 1.5, 3.0, 4.5, 8.6$ (lines) and experimental data [8] for $\bar{B} = 0.2, 0.5, 0.7, 1.4$ [T] (empty symbols). We have adjusted the maximum values of the torque curves and displayed those curves with changing its maximum values arbitrarily to be clearly seen. The highest field theoretical data $\bar{B} = 8.6$ and experimental data 1.4 [T] clearly show the jumps associated with the first order transition. (b) Maximum angles of the form factors (triangles) and the torque curves (circles) in the \bar{B} and angle θ plane. Theoretical results (filled symbols) are compared with the corresponding experimental data [4, 8] (empty symbols). In the scale of vertical axis, $H_{c2,ab} = 9.1$ in theoretical estimate is assigned to be 1.5 [T].

der the experimental values. This can be easily remedied by changing the μ value. Namely, instead of the present value $\mu = 0.04$, the refined value $\mu = 0.0293$ shows much better fitting to the experimental data by Eq. (A3), as shown in Figs. 11(b) and 11(c).

We also evaluate the temperature dependence of the ratio $\Gamma_{H_{c2}}(T) \equiv H_{c2,ab}(T)/H_{c2,c}(T)$, and compare it with the experimental data [67] in Fig. 11(d). Near $T = T_c$, both in numerical and experimental data, $\Gamma_{H_{c2}}(T)$ shows the large anisotropy ratio, tending to ~ 60 , which is governed by the Fermi velocity anisotropy ratio of the β band $\Gamma_\beta = 57$. Upon decreasing T , this ratio progressively becomes small because of the PPE. This is captured by our numerical calculation, and the tending limit towards the lowest T is 16. The T -dependence is well fitted by Eq. (A3) with Eq. (A4) for $\mu = 0.04$, as shown in Fig. 11(d). In the experimental data which reduces 20

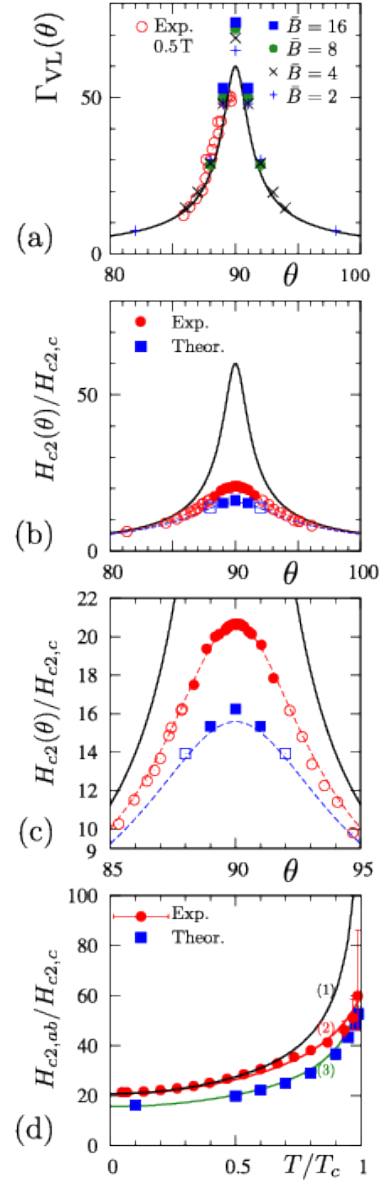


FIG. 11: (Color online) (a) The θ -dependences of the vortex lattice anisotropy $\Gamma_{VL}(\theta)$. Open circles indicate the experimental data for $B=0.5$ [T] [4]. Other symbols are for $\Gamma_{VL}(\theta)$ evaluated by the free energy minimum at $\bar{B}/B_0 = 2, 4, 8,$ and 16 for $\mu = 0$. The line presents $\Gamma(\theta)$ of the effective mass model in Eq. (9) with $\Gamma = 60$. (b) The θ -dependences of $H_{c2}(\theta)/H_{c2,c}$ at $T = 0.1T_c$ for $\mu = 0.04$. (c) Enlarged figure of (b). The results of numerical calculations by Eilenberger theory are presented by square points. The experimental data[8] are shown by circles. There, the filled (empty) symbols indicate the first (second) order transition. The solid line shows $\Gamma(\theta)$ of the effective mass model with $\Gamma = 60$. The dashed lines correspond to the theoretical curves calculated by Eq. (A3) with $\Gamma = 60$, where $\mu = 0.04$ for fitting to numerical calculations and $\mu = 0.0293$ for fitting to experimental data. (d) The anisotropy $\Gamma_{H_{c2}}(T) = H_{c2,ab}(T)/H_{c2,c}(T)$ as a function of T . The experimental data[67] (circles) and the numerical results by Eilenberger theory with $\mu = 0.04$ (squares) are shown. The three continuous lines are evaluated by Eqs. (A3) and (A4) with (1) $\Gamma = 180$ and $\mu = 0.0293$, (2) $\Gamma = 60$ and $\mu = 0.0293$, and (3) $\Gamma = 60$ and $\mu = 0.04$.

at low T [67] is fitted by Eq. (A3) with $\mu=0.0293$ as in the case of Figs. 11(b) and 11(c). We also note that the fitting line with $\Gamma = 180$ largely deviates from the experimental data. A similar analysis on the H_{c2} anisotropy data [67] is performed by Choi [36] to come to the same conclusion. We point out again that in numerical calculation (blue square) the point in low T range in Fig. 11(d) corresponds to the first order $H_{c2,ab}$ transition, while at least above $T/T_c > 0.5$, $H_{c2,ab}$ is of second order. According to the experiments [7, 8], the first order line at $H_{c2,ab}(T)$ extends to around $T/T_c > 0.4 \sim 0.5$. The accurate termination point between the first and second order transitions will be a future problem.

In summary of this section, in both estimations of $\Gamma_{VL}(\theta)$ and $\Gamma_{H_{c2}}(T)$, the intrinsic anisotropy Γ of Sr_2RuO_4 is identified as $\Gamma = 60$. Since it corresponds to $\Gamma_\beta = 57$ given by the β band among the known three bands. The anisotropy $\Gamma = 60$ indicates that the β band is fully responsible for determining various observables. Thus this should be the major band, while the γ band with $\Gamma_\gamma = 174$ is not appropriate for the major band as seen from Fig. 11(d) and must be the minority band and the α band plays a negligible role because its DOS is 10% of the total. Those considerations partly justify the present single band model to grasp the essential points.

IX. CONCLUSION AND UNSOLVED PROBLEMS

The essential assumption in the present theory is that the PPE works in the spin part of the pairing function. The assumption for the orbital part as isotropic s -wave is not intrinsic in our calculations. As the pairing function inducing the PPE, in addition to the spin-singlet pairing, the spin-triplet pairing is also available if the d -vector has components in the ab plane.

There exist several outstanding experiments to claim as the evidence for a spin-triplet chiral p -wave pairing realizing in Sr_2RuO_4 . Among them, only the Knight shift experiments [13–16] by NMR and polarized neutron scattering are treated as an evidence for that the spin part of the pairing function is the spin-triplet. There the Knight shift remains unchanged for any magnetic field orientations, any H , T and any nuclear species available so far. These are against the present theory. However, the unchanged T -dependence for all field orientations is a mystery, since the Knight shift is expected to be decreased for some of field orientations even in the spin-triplet pairing.

Other experiments than the Knight shift are evidences for the orbital part of the pairing. There, the time reversal symmetry breaking is suggested by muon spin rotation (μSR) [40], which shows the appearance of the spontaneous moments below T_c . These varieties of the orbital part can be easily accommodated in the present theoretical framework. As for the time reversal symmetry breaking, the possible pairing can be an $s + id$ or $d + id$ in the spin-singlet pairing, or $p_x + ip_y$ in the

spin-triplet pairing. Even in the spin-triplet pairing, the PPE works if the d -vector has a component within the ab plane. The essential characteristics of the mixed state magnetic properties investigated here remains intact even for those pairings. In the present paper we have taken the isotropic s -wave just for computational convenience and for the illustrative purpose.

From the results that the PPE plays significant contributions on the superconducting properties for $\vec{\mathbf{B}} \parallel ab$, we recognize the importance of the further studies to determine the spin part of the pairing function. In Sr_2RuO_4 , due to the spin-orbit coupling of the electronic states, we have to consider the coupling of the spin and the orbital parts in the spin-triplet pairing function [22, 68–70]. This may be an essential factor to realize a spin-triplet superconductor where the d -vector has the component in the ab plane.

Several important experimental facts remain unanswered in the present theory:

(1) As shown in Fig. 5(c), the transverse form factors as a function of θ under a fixed field in the SANS experiment [4] exhibit a strong decay of its amplitudes long before reaching the expected H_{c2} , when θ decreases away from the ab plane at $\theta = 90^\circ$ in the lower fields. We anticipate the interplay of the multiband effect to explain it [65].

(2) It is also obvious that the $\gamma(H)$ behavior shown in Fig. 6(d) is quite different from the observed C/T at low T especially at lower field regions [71] where a \sqrt{H} -like sharp increase is observed. This was interpreted as coming from the minor band ($\alpha + \beta$) that is assumed to have a line node like gap structure simply because the DOS value attained in that field region seems to that for the $\alpha + \beta$ bands (43% of the total DOS). The γ band with 57% of the total DOS is regarded as the major band.

This interpretation is at odds with the present theory in several points; If this is true, the “major” γ band should be responsible for the high field region. Since the Fermi velocity anisotropy $\Gamma_\gamma = 174$ for the γ band, we would expect $\Gamma_{VL} \sim 174$ for $\vec{\mathbf{B}} \parallel ab$. There is no indication for it in the available SANS data [4] and other [67]. Instead, the SANS data [4] $\Gamma_{VL} \sim 60$ indicate that the high field phase should be the β band. We point out also the data [67] $H_{c2,ab}(T)/H_{c2,c}(T)$ shown in Fig. 11(d) which is directly related to the Fermi velocity anisotropy in Eq. (1) near T_c . Thus the β band is also responsible for it [65]. There is no trace in the existing data to show that the γ band plays a major role. The present single band theory assumes the β band as the major band, neglecting the minor γ band. We need to refine it by taking into account both bands in addition to the remaining α band. A multiband theory based on Eilenberger framework belongs to a future work [65].

In order to further advance the Sr_2RuO_4 problem concerning its pairing symmetry and multiband nature, we propose here several decisive experiments:

(A) The SANS experiments to observe the longitudinal component F_z in the FLL form factors. As already pre-

dicted in Figs. 4 and 5(c) the magnitudes $F_{z(1,0)}$ and $F_{z(1,1)}$ near H_{c2} are within the observable range. We expect to see the enhanced F_z behavior towards H_{c2} , a similar behavior already observed in CeCoIn₅ [56] which is known to be a typical superconductor with strong PPE. (B) To determine the detailed gap structure on the α , β and γ bands the field angle resolved specific heat experiment is decisive. The existing data [71] at low fields are only down to 100 mK which was concluded to have a d_{xy} like nodal structure, judging from the existing four fold oscillation pattern. We expect that the sign of the four fold oscillation in C/T might change because the γ band responsible for this oscillation at low fields and low temperatures should have a $d_{x^2-y^2}$ like nodal structure. Such a sign change of the oscillation has been observed in CeCoIn₅ [72]. This $d_{x^2-y^2}$ like nodal structure on the γ band is fully consistent with other experiments. In particular, the square vortex lattice pattern oriented to (110) direction is observed for $\mathbf{B} \parallel c$ in the SANS experiments [58]. Note in passing that the gap structures of β and α bands are relatively isotropic [65]. This might be consistent with the c -axis tunneling data [73] that probes selectively the β band with the least Fermi velocity along this direction and shows a full gap.

(C) Finally according to the present theory with PPE, Sr₂RuO₄ is quite likely to exhibit the Fulde-Ferrell-Larkin-Ovchinnikov (FFLO) phase in low T and high H regions just below H_{c2} . One of the best way to detect it is to measure T_1^{-1} by NMR, which is enhanced in the FFLO phase. This method is successfully applied to the organic superconductor κ -(BEDT-TTF)₂Cu(NCS)₂ [74].

In summary, we investigate the mixed state properties of a uniaxially anisotropic superconductor with the Pauli paramagnetic effect on the basis of microscopic Eilenberger theory in the clean limit, assuming a single band model. By these studies, we discussed the field orientation dependence near $\mathbf{B} \parallel ab$, and tried to explain curious behaviors in Sr₂RuO₄, focusing on contributions by the Pauli-paramagnetic effect. In the study of the longitudinal and transverse components of the flux line lattice form factors, effects of $H_{c2,ab}$ suppression due to the paramagnetic pair breaking is important to quantitatively explain the intensity of the spin-flip SANS experiment observed in Sr₂RuO₄ [4]. In the magnetization curve and field-dependent Sommerfeld coefficient, the jumps at the first order $H_{c2,ab}$ transition mainly come from the contribution of the paramagnetic susceptibility. From the study on the field orientation dependence of torque curves and $H_{c2}(\theta)$, the intrinsic anisotropy ratio between c and ab directions is $\Gamma \sim 60$, suggesting the main contribution of the β -band in the superconductivity of Sr₂RuO₄. These consistent behaviors between experimental observation and the theoretical calculation indicate that the Pauli paramagnetic effect plays important roles to understand curious behaviors at high fields for $\mathbf{B} \parallel ab$ in Sr₂RuO₄. This suggests that the pairing symmetry is either a spin-singlet or a spin-triplet pairing with the d -vector components in the ab plane. We

expect further experimental and theoretical future studies to confirm the mechanism of high field behaviors for $\mathbf{B} \parallel ab$ in Sr₂RuO₄.

Acknowledgments

We thank T. Sakakibara, S. Kittaka, A. Kasahara, S. Yonezawa, Y. Maeno, M. R. Eskildsen, K. Ishida and Y. Matsuda for fruitful discussions and support from the experimental side.

Appendix A

According to Ref. 66, an analytic expression for the μ -dependence of the upper critical field $H_{c2}(\mu)$ was derived by the fitting to the numerical solutions of Eilenberger equation under PPE at low temperatures. The expression for $H_{c2}(\theta, \mu)$ is given by

$$\frac{H_{c2}(\theta, \mu)}{H_{c2}^{\text{orb}}(\theta)} = \frac{1}{\sqrt{1 + 2.4\tilde{\mu}(\theta)^2}} \quad (\text{A1})$$

for each field orientation θ in a uniaxial superconductor. There $H_{c2}^{\text{orb}}(\theta) = H_{c2}(\theta, \mu = 0) = H_{c2,c}^{\text{orb}}\Gamma(\theta)$ is the orbital limited upper critical field without PPE. The effective paramagnetic parameter $\tilde{\mu}(\theta)$ at each θ depends on anisotropy $\Gamma(\theta)$ in Eq. (9) as

$$\tilde{\mu}(\theta) = \mu \frac{H_{c2}^{\text{orb}}(\theta)}{H_{c2,c}^{\text{orb}}} = \mu\Gamma(\theta), \quad (\text{A2})$$

since $\tilde{\mu}(\theta) \propto H_{c2}^{\text{orb}}(\theta)/H_p$. The Pauli paramagnetic critical field H_p is proportional to the pair potential Δ at a zero field. By combining Eqs. (A1) and (A2), we obtain

$$\frac{H_{c2}(\theta, \mu)}{H_{c2,c}^{\text{orb}}} = \frac{1}{\sqrt{\cos^2\theta + \Gamma^{-2}\sin^2\theta + 2.4\mu^2}}. \quad (\text{A3})$$

This gives the θ -dependent $H_{c2}(\theta)$ in Figs. 11(b) and 11(c). When we evaluate the T -dependence of $H_{c2}(\theta, \mu)/H_{c2,c}^{\text{orb}}$ in Eq. (A3), $\mu = \mu(T = 0)$ is modified to the T -dependent paramagnetic parameter $\mu(T)$ given by

$$\mu(T) = \mu \frac{\Delta(0)}{\Delta(T)} \frac{H_{c2,c}^{\text{orb}}(T)}{H_{c2,c}^{\text{orb}}(0)}. \quad (\text{A4})$$

The T -dependent orbital limited $H_{c2,c}^{\text{orb}}(T)$ is given by the Werthamer-Helfand-Hohenberg (WHH) formula [75] or the solution of the Eilenberger equation in the clean limit. The T -dependent order parameter $\Delta(T)$ follows the BCS form. The T -dependence of H_{c2} anisotropy $H_{c2,ab}(T)/H_{c2,c}(T)$ when $\theta = 90^\circ$ is obtained by Eqs. (A3) and (A4), which is displayed in Fig. 11(d).

- [1] A. P. Mackenzie and Y. Maeno, *Rev. Mod. Phys.* **75**, 657 (2003).
- [2] Y. Maeno, S. Kittaka, T. Nomura, S. Yonezawa, and K. Ishida, *J. Phys. Soc. Jpn.* **81**, 011009 (2012).
- [3] C. Bergemann, A. P. Mckenzie, S.R. Jurian, D. Forsythe, and E. Ohmichi, *Adv. Phys.* **52**, 639 (2003).
- [4] C. Rastovski, C. D. Dewhurst, W. J. Gannon, D. C. Peets, H. Takatsu, Y. Maeno, M. Ichioka, K. Machida, and M. R. Eskildsen, *Phys. Rev. Lett.* **111**, 087003 (2013).
- [5] In multi-band superconductors such as MgB₂, this relation may be modified. See, for example, P. Miranović, K. Machida, and V. G. Kogan, *J. Phys. Soc. Jpn.* **72**, 221 (2003).
- [6] S. Yonezawa, T. Kajikawa, and Y. Maeno, *Phys. Rev. Lett.* **110**, 077003 (2013).
- [7] S. Yonezawa, T. Kajikara, and Y. Maeno, *J. Phys. Soc. Jpn.* **83**, 083706 (2014).
- [8] S. Kittaka, A. Kasahara, T. Sakakibara, D. Shibata, S. Yonezawa, Y. Maeno, K. Tenya, and K. Machida, *Phys. Rev. B* **90**, 220502 (R) (2014).
- [9] T. Tayama, A. Harita, T. Sakakibara, Y. Haga, H. Shishido, R. Settai, and Y. Onuki, *Phys. Rev. B* **65**, 180504 (R) (2002).
- [10] K. Kakuyanagi, M. Saitoh, K. Kumagai, S. Takashima, M. Nohara, H. Takagi, and Y. Matusda, *Phys. Rev. Lett.* **94**, 047602 (2005).
- [11] K. Kumagai, H. Shishido, T. Shibauchi, and Y. Matsuda, *Phys. Rev. Lett.* **106**, 137004 (2011).
- [12] A. D. Bianchi, M. Kenzelmann, L. DeBeer-Schmitt, J. S. White, E. M. Forgan, J. Mesot, M. Zolliker, J. Kohlbrecher, R. Movshovich, E. Bauer, J. Sarrao, Z. Fisk, C. Perovic, and M. R. Eskildsen, *Science* **319**, 177 (2008).
- [13] K. Ishida, H. Mukuda, Y. Kitaoka, K. Asayama, Z. Q. Mao, Y. Mori, and Y. Maeno, *Nature* **396**, 658 (1998).
- [14] H. Murakawa, K. Ishida, K. Kitagawa, Z. Q. Mao, and Y. Maeno, *Phys. Rev. Lett.* **93**, 167004 (2004).
- [15] K. Ishida, H. Murakawa, H. Mukuda, Y. Kitaoka, Z. Q. Mao, Y. Maeno, *J. Phys. Chem. Solids*, **69**, 3108 (2008).
- [16] J. A. Duffy, S. M. Hayden, Y. Maeno, Z. Mao, J. Kulda, and G. J. McIntyre, *Phys. Rev. Lett.* **85**, 5412 (2000).
- [17] T. M. Rice and M. Sigrist, *J. Phys.: Condens. Matter* **7**, L643 (1995).
- [18] M. E. Zhitomirsky and T. M. Rice, *Phys. Rev. Lett.* **87**, 057001 (2001).
- [19] J. F. Annett, G. Litak, B. L. Györfy, and K. I. Wysokiński, *Phys. Rev. B* **66**, 134514 (2002).
- [20] T. Nomura and K. Yamada, *J. Phys. Soc. Jpn.* **69**, 3678 (2000). T. Nomura and K. Yamada, *J. Phys. Soc. Jpn.* **71**, 404 (2002). T. Nomura and K. Yamada, *J. Phys. Soc. Jpn.* **71**, 1993 (2002).
- [21] S. Koikegami, Y. Yoshida, and T. Yanagisawa, *Phys. Rev. B* **67**, 134517 (2003).
- [22] Y. Yanase and M. Ogata, *J. Phys. Soc. Jpn.* **72**, 673 (2003).
- [23] P. Thalmeir and K. Maki, *Acta Phys. Pol. B* **34**, 557 (2003).
- [24] T. Kuwabara and M. Ogata, *Phys. Rev. Lett.* **85**, 4586 (2000).
- [25] M. Sato and M. Kohmoto, *J. Phys. Soc. Jpn.* **69**, 3505 (2000).
- [26] K. Kuroki, M. Ogata, R. Arita, and H. Aoki, *Phys. Rev. B* **63**, 060506 (R) (2001).
- [27] T. Takimoto, *Phys. Rev. B* **62**, 14641 (R) (2000).
- [28] T. Dahm, H. Won, and K. Maki, *cond-mat/0006301*.
- [29] W. C. Wu and R. Joynt, *Phys. Rev. B* **64**, 100507 (R) (2001).
- [30] I. Eremin, D. Manske, C. Joas, and K. H. Bennemann, *Europhys. Lett.* **58**, 871 (2002).
- [31] K. Miyake and O. Narikiyo, *Phys. Rev. Lett.* **83**, 1423 (1999).
- [32] Y. Hasegawa and M. Yakiyama, *J. Phys. Soc. Jpn.* **72**, 1318 (2003).
- [33] K. Kubo and D. S. Hirashima, *J. Phys. Soc. Jpn.* **69**, 3489 (2000).
- [34] H. Won and K. Maki, *Europhys. Lett.* **52**, 427 (2000).
- [35] M. J. Graf and A. V. Balatsky, *Phys. Rev. B* **62**, 9697 (2000).
- [36] C-H. Choi, *J. Korean Phys. Soc.* **56**, 933 (2010).
- [37] J. Zhang, C. Lörscher, Q. Gu, and R. A. Klemm, *J. Phys.: Condens. Matter* **26**, 252201(2014).
- [38] H. Hasegawa, K. Machida, and M. Ozaki, *J. Phys. Soc. Jpn.* **69**, 336 (2000). K. Machida, M. Ozaki, and T. Ohmi, *J. Phys. Soc. Jpn.* **65**, 3720 (1996). M. Ozaki, K. Machida, and T. Ohmi, *Prog. Theor. Phys.* **76**, 442 (1986).
- [39] J. Jang, D. G. Ferguson, V. Vararyuk, R. Budakian, S. B. Chung, P. M. Goldbert, and Y. Maeno, *Science* **331**, 186 (2011).
- [40] G. M. Luke, Y. Fudamoto, K. M. Kojima, M. L. Larkin, J. Merrin, B. Nachumi, Y. J. Uemura, Y. Maeno, Z. Q. Mao, Y. Mori, H. Nakamura, and M. Sigrist, *Nature (London)* **394**, 558 (1998).
- [41] F. Kidwingira, J. D. Strand, D. J. Van Harlingen, and Y. Maeno, *Science* **314**, 1267 (2006).
- [42] S. Kashiwaya, H. Kashiwaya, H. Kambara, T. Furuta, H. Yaguchi, Y. Tanaka, and Y. Maeno, *Phys. Rev. Lett.* **107**, 077003 (2011).
- [43] J. R. Kirtley, C. Kallin, C. W. Hicks, E. A. Kim, Y. Liu, K. A. Moler, Y. Maeno, and K. D. Nelson, *Phys. Rev. B* **76**, 014526 (2007).
- [44] C. Kallin and A. J. Berlinsky, *J. Phys.: Condens. Matter* **21**, 164210 (2009). C. Kallin, *Rep. Prog. Phys.* **75**, 042501 (2012).
- [45] M. Ichioka and K. Machida, *Phys. Rev. B* **76**, 064502 (2007); M. Ichioka, K. M. Suzuki, Y. Tsutsumi, and K. Machida, in *Superconductivity - Theory and Applications*, edited by A. M. Luiz (InTech, Croatia, 2011), Chap.10.
- [46] M. Ishihara, Y. Amano, M. Ichioka, and K. Machida, *Phys. Rev. B* **87**, 224509 (2013).
- [47] Y. Amano, M. Ishihara, M. Ichioka, N. Nakai, and K. Machida, *Phys. Rev. B* **90**, 144514 (2014).
- [48] M. Hiragi, K.M. Suzuki, M. Ichioka, and K. Machida, *J. Phys. Soc. Jpn.* **79**, 094709 (2010).
- [49] P. Miranović, M. Ichioka, and K. Machida, *Phys. Rev. B* **70**, 104510 (2004).
- [50] U. Klein, *J. Low Temp. Phys.* **69**, 1 (1987).
- [51] W. Pesch, *Z. Phys. B* **21**, 263 (1975).
- [52] K. Watanabe, T. Kita, and M. Arai, *Phys. Rev. B* **71**, 144515 (2005).
- [53] M. M. Doria, J. E. Gubernatis, and D. Rainer, *Phys.*

- Rev. B **41**, 6335 (1990).
- [54] P. G. Kealey, D. Charalambous, E. M. Forgan, S. L. Lee, S. T. Johnson, P. Schleger, R. Cubitt, D. McK. Paul, C. M. Aegerter, S. Tajima, and A. Rykov, Phys. Rev. B **64**, 174501 (2001).
- [55] S. L. Thiemann, Z. Radović, and V. G. Kogan, Phys. Rev. B **39**, 11406 (1989).
- [56] J. S. White, P. Das, M. R. Eskildsen, L. DeBeer-Schmitt, E. M. Forgan, A. D. Bianchi, M. Kenzelmann, M. Zolliker, S. Gerber, J. L. Gavilano, J. Mesot, R. Movshovich, E. D. Bauer, J. L. Sarrao, and C. Petrovic, New J. Phys. **12**, 023026 (2010).
- [57] L. DeBeer-Schmitt, M. R. Eskildsen, M. Ichioka, K. Machida, N. Jenkins, C. D. Dewhurst, A. B. Abrahamson, S. L. Bud'ko, and P. C. Canfield, Phys. Rev. Lett. **99**, 167001 (2007).
- [58] T. M. Riseman, P. G. Kealey, E. M. Forgan, A. P. Mackenzie, L. M. Galvin, A. W. Tyler, S. L. Lee, C. Ager, D. McK. Paul, C. M. Aegerter, R. Cubitt, Z. Q. Mao, T. Akima, and Y. Maeno, Nature (London) **396**, 242 (1998) [note correction: Nature(London) **404**, 629 (2000)]. P. G. Kealey, T. M. Riseman, E. M. Forgan, L. M. Galvin, A. P. Mackenzie, S. L. Lee, D. McK. Paul, R. Cubitt, D. F. Agterberg, R. Heeb, Z. Q. Mao, and Y. Maeno, Phys. Rev. Lett. **84**, 6094 (2000).
- [59] M. Ichioka, A. Hasegawa, and K. Machida, Phys. Rev. B **59**, 8902 (1999). M. Ichioka, A. Hasegawa, and K. Machida, Phys. Rev. B **59**, 184 (1999).
- [60] M. Takigawa, M. Ichioka, and K. Machida, Phys. Rev. Lett. **83**, 3057 (1999). M. Takigawa, M. Ichioka, and K. Machida, J. Phys. Soc. Jpn. **69**, 3943 (2000).
- [61] K. K. Tanaka, M. Ichioka, N. Nakai, and K. Machida, Phys. Rev. B **89**, 174504 (2014).
- [62] A. Yaouanc, A. Maisuradze, N. Nakai, K. Machida, R. Khasanov, A. Amato, P. K. Biswas, C. Baines, D. Hurlach, R. Henes, P. Keppler, and H. Keller, Phys. Rev. B **89**, 184503 (2014).
- [63] C. M. Aegerter, S. H. Lloyd, C. Ager, S. L. Lee, S. Romer, H. Keller, and E. M. Forgan, J. Phys.: Condens. Matter **10**, 7445 (1998).
- [64] V. G. Kogan, Phys. Rev. Lett. **89**, 237005 (2002).
- [65] N. Nakai, *et al.*, in preparation.
- [66] K. Machida and M. Ichioka, Phys. Rev. B **77**, 184515 (2008).
- [67] S. Kittaka, T. Nakamura, Y. Aono, S. Yonezawa, K. Ishida, and Y. Maeno, Phys. Rev. B **80**, 174514 (2009). S. Kittaka, T. Nakamura, Y. Aono, S. Yonezawa, K. Ishida, and Y. Maeno, J. Phys.: Conf. Ser. **150**, 052112 (2009).
- [68] K.K. Ng and M. Sigrist, Europhys. Lett. **49**, 473 (2000).
- [69] T. Scaffidi, J. C. Romers, and S. H. Simon, Phys. Rev. B **89**, 220510(R) (2014).
- [70] M. Tsuchiizu, Y. Yamakawa, S. Onari, Y. Ohno, and H. Kontani, Phys. Rev. B **91**, 155103 (2015).
- [71] K. Deguchi, Z. Q. Mao, and Y. Maeno, J. Phys. Soc. Jpn. **73**, 1313 (2004).
- [72] K. An, T. Sakakibara, R. Settai, Y. Onuki, M. Hiragi, M. Ichioka, and K. Machida, Phys. Rev. Lett. **104**, 037002 (2010).
- [73] H. Suderow, V. Crespo, I. Guillamon, S. Vieira, F. Servant, P. Lejay, J. P. Brison, and J. Flouquet, New J. Phys. **11**, 093004 (2009).
- [74] H. Mayaffre, S. Krämer, M. Horvatić, C. Berthier, K. Miyagawa, K. Kanoda, and V. F. Mitrović, Nature Phys. **10**, 928 (2014).
- [75] N. R. Werthamer, E. Helfand, and P. C. Hohenberg, Phys. Rev. **147**, 295 (1966).